PASJ: Publ. Astron. Soc. Japan **60**, S435–S451, 2008 December 25

AKARI IRC Survey of the Large Magellanic Cloud: Outline of the Survey and Initial Results

Yoshifusa ITA,[1] Takashi ONAKA,[2] Daisuke KATO,[2] Toshihiko TANABÉ,[3] Itsuki SAKON,[2] Hidehiro KANEDA,[4] Akiko KAWAMURA,[5] Takashi SHIMONISHI,[2] Takehiko WADA,[4] Fumihiko USUI,[4] Bon-Chul KOO,[6] Mikako MATSUURA,[1] Hidenori TAKAHASHI,[7] Yoshikazu NAKADA,[3] Tetsuo HASEGAWA,[1] and Motohide TAMURA[1]

[1]*National Astronomical Observatory of Japan, 2-21-1 Osawa, Mitaka, Tokyo, 181-8588*
yoshifusa.ita@nao.ac.jp
[2]*Department of Astronomy, School of Science, The University of Tokyo, 7-3-1 Hongo, Bunkyo-ku, Tokyo 113-0033*
[3]*Institute of Astronomy, School of Science, The University of Tokyo, 2-21-1 Osawa, Mitaka, Tokyo 181-0015*
[4]*Institute of Space and Astronautical Science, Japan Aerospace Exploration Agency, 3-1-1 Yoshinodai, Sagamihara, Kanagawa 229-8510*
[5]*Department of Astrophysics, Nagoya University, Chikusa-ku, Nagoya 464-8602*
[6]*Department of Physics and Astronomy, Seoul National University, Seoul 151-742, Korea*
[7]*Gunma Astronomical Observatory, 6860-86 Nakayama, Takayama, Agatsuma, Gunma 377-0702*

(Received 2008 May 16; accepted 2008 August 21)

Abstract

We observed an area of 10 deg^2 of the Large Magellanic Cloud using the Infrared Camera (IRC) on board AKARI. The observations were carried out using five imaging filters (3, 7, 11, 15, and 24 μm) and a dispersion prism (2–5 μm, $\lambda/\Delta\lambda \sim 20$) equipped in the IRC. This paper describes an outline of our survey project, and presents some initial results using imaging data that detected over 5.9×10^5 near-infrared and 6.4×10^4 mid-infrared point sources. The 10 σ detection limits of our survey are about 16.5, 14.0, 12.3, 10.8, and 9.2 in Vega-magnitude at 3, 7, 11, 15, and 24 μm, respectively. The 11 and 15 μm data, which are unique to AKARI IRC, allow us to construct color–magnitude diagrams that are useful to identify stars with circumstellar dust. We found a new sequence in the color–magnitude diagram, which is attributed to red giants with luminosity fainter than that of the tip of the first red-giant branch. We suggest that this sequence is likely to be related to the broad emission feature of aluminum oxide at 11.5 μm. The 11 and 15 μm data also indicate that the (*[11]–[15]*) color of both oxygen-rich and carbon-rich red giants once becomes blue, and then turns red again in the course of their evolution, probably due to a change in the flux ratio of the silicate or silicon carbide emission feature at 10 or 11.3 μm to the 15 μm flux.

Key words: galaxies: Magellanic Clouds — infrared: stars — ISM: supernova remnants — stars: AGB and post-AGB-young stellar objects

1. Introduction

Owing to its proximity ($\sim$ 50 kpc: e.g., Feast & Walker 1987) and face-on geometry, the Large Magellanic Cloud (LMC) is an ideal natural laboratory to study various astrophysical fields. It is located at a high galactic latitude of $\sim -36°$, and we expect less contamination of foreground stars and less interstellar extinction. It is far enough away to neglect its depth, so that we can reasonably assume that objects in the LMC are all at the same distance from us. The apparent size of the LMC is also such that can be surveyed in a reasonable amount of time to study the material circulation processes and star-formation history on a galactic scale. Meanwhile, it is close enough to resolve and study individual objects, even with relatively small telescopes. Moreover, the mean metallicity of the LMC is known to be small ($\sim 1/4$) compared to solar abundance, intriguing us to study the influence of low metallicity on various astrophysical phenomena.

Because of these characteristics, there have been a number of survey projects of the LMC at various wavelengths (Hard X-ray: Götz et al. 2006; Soft X-ray: e.g., Long et al. 1981 with Einstein; Sasaki et al. 2000; Haberl & Petsch 1999 with ROSAT; and Haberl et al. 2003 with XMM; UV: Smith et al. 1987; Hα: Kennicutt & Hodge 1986; Gaustad et al. 2001; Optical: Zaritsky et al. 2004; NIR: e.g., Cioni et al. 2000a with DENIS; Nikolaev & Weinberg 2000 with 2MASS; and Kato et al. 2007 with IRSF / SIRIUS; MIR & FIR: e.g., Israel & Schwering 1986 with IRAS; Egan et al. 2003 with MSX; and Meixner et al. 2006 with Spitzer/SAGE; [C II]: Mochizuki et al. 1994; CO: e.g., Mizuno et al. 2001 with NANTEN; H I: Luks & Rohlfs 1992; Kim et al. 1998).

A ground-based near-infrared (NIR) survey detected about fifteen million sources in the $\sim$40 deg^2 area of the LMC (Kato et al. 2007). On the other hand, previous mid-infrared (MIR) surveys detected only a few thousands sources in an $\sim$100 deg^2 area of the LMC (Egan et al. 2003), which is too shallow to compare with survey observations at other wavelengths. Moreover, the angular resolutions of previous MIR surveys were not high enough to make secure cross-identifications with other survey catalogs. This situation has been significantly improved with the advent of the Spitzer Space Telescope (SST: Werner et al. 2004) and AKARI, which have instruments capable of deep mid-infrared observations with the high spatial resolution. The Spitzer SAGE project (Meixner et al. 2006) carried out a uniform and unbiased imaging survey of about 49 deg^2 area of the LMC, providing photometry for about

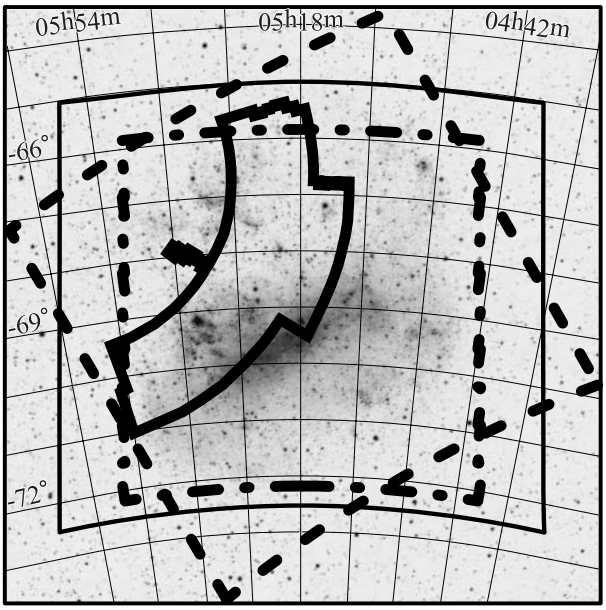

Fig. 1. Observed area of the AKARI IRC survey (thick solid outline), overlaid on a photographic image kindly provided by Mr. Motonori Kamiya. The thick dashed outline indicates the coverage of the Spitzer / SAGE survey ($7^\circ \times 7^\circ$: Meixner et al. 2006), the thick dash-doted outline shows the coverage of the IRSF / SIRIUS near-infrared survey ($6.^\circ3 \times 6.^\circ3$: Kato et al. 2007), and the thin solid outline represents the coverage of the Magellanic clouds optical photometric survey ($8.^\circ5 \times 7.^\circ5$: Zaritsky et al. 2004).

2×10^5 sources with all IRAC (Fazio et al. 2004a) bands at two epochs separated by 3 months.

We carried out near- to mid-infrared imaging and a near-infrared spectroscopic survey toward the LMC with AKARI (figure 1). The entire LMC was also observed as being part of the All-Sky Survey at 6 bands in the mid- to far-infrared regions with AKARI (Ishihara et al. 2006; Kawada et al. 2007). AKARI observations provide multi-band (11 bands) data of the LMC from the near- to far-infrared (FIR), which will give us a new insight into the various phenomena occurring in the LMC. In this paper, we provide an overview of our LMC survey project, and present some initial results using the preliminary photometric catalog of bright point sources.

We then will make general analyses using the catalog with an emphasis on the unique characteristics of the Infrared Camera (IRC) observations compared to the Spitzer observations. The first AKARI / IRC LMC point-source catalog is planned to be released to the public in 2009.

2. The AKARI IRC LMC Survey Project

The Japan Aerospace Exploration Agency launched an Infrared Satellite, ASTRO-F (Murakami et al. 2007), at 21:28 UTC on 2006 February 21 from the Uchinoura Space Center. Once in orbit, ASTRO-F was renamed "AKARI". AKARI has a 68.5 cm telescope and two scientific instruments, namely the InfraRed Camera (IRC: Onaka et al. 2007) and the Far-Infrared Surveyor (FIS: Kawada et al. 2007). Both instruments have low- to moderate-resolution spectroscopic capability. The IRC has nine imaging bands and six dispersive elements covering a wavelength range from 2.5 to 26 μm. (Unfortunately, one of the dispersive elements that was expected to cover the 11 to 19 μm range became opaque during ground test operation, and become defunct in orbit). The FIS will observe in the 4 far-infrared bands between 50 and 180 μm. One of the primary goals of the AKARI mission is to carry out an All-Sky Survey with the FIS and the IRC at six bands from 9 to 180 μm (Ishihara et al. 2006; Kawada et al. 2007). As a result, the entire LMC has been mapped in the 9, 18, 65, 90, 140, and 160 μm wavebands. The 5 σ detection limits for one scan observation of the All-Sky Survey are shown in figure 3. As described below, the LMC is located at a relatively high visibility region for AKARI's orbit. AKARI scanned LMC several times, and thus better detection limits should be obtained by further data reduction of the All-Sky Survey data. The All-Sky Survey observations of the LMC will be described elsewhere, and are not discussed in this paper.

In addition to the All-Sky Survey in mid- and far-infrared, AKARI carried out two large-area legacy surveys (LS) in the pointing mode. The LMC survey project (PI. T. Onaka) is one of two LS programs. The other is the North Ecliptic Pole survey project (PI. H. Matsuhara: Matsuhara et al. 2007). These survey areas are located at high ecliptic latitudes, where the visibility is high for AKARI's Sun-synchronous polar orbit. Therefore, a batch of observing times can be allocated for pointing observations in these areas after allocating scan paths for the All-Sky Survey. We used the IRC to make imaging and spectroscopic mapping observations of the main part of the LMC.

The IRC is comprised of three independent channels (NIR, MIRS, and MIRL), which cover the 1.8–5.5 μm, 4.6–13.4 μm, and 12.6–26.5 μm wavelength ranges, respectively. Each of the three channels has three imaging bands and two dispersion elements, which can be switched during a pointed observation opportunity. Each of the channels has a wide field of view (FOV) of about $10' \times 10'$, suitable for survey observations. Compared to the contemporary SST, the AKARI IRC has the following characteristics:

- The IRC's imaging filters cover the wavelength range continuously from 2.5 to 26 μm. In particular, it has 11μm (*S11*) and 15μm (*L15*) imaging bands, which fill the gap between the IRAC (Fazio et al. 2004a) and MIPS (Rieke et al. 2004) aboard the SST. The wavelength range that the *S11* and *L15* bands cover contains interesting spectral features, such as the silicate 10 and 18 μm bands. Figure 2 shows the spectral response functions of the IRC, IRAC, and MIPS bands, together with the ISO-SWS spectra (Sloan et al. 2003) of an oxygen-rich AGB star (VX Sgr) and a carbon-rich AGB star (IRC +50096). IRC *S11* and *L15* probe the silicate bands efficiently.
- One of the most significant features of the IRC is its ability to perform slit-less spectroscopy in addition to imaging. It can simultaneously obtain near- to mid-infrared (about 2–13 μm) continuous spectra of all sources present in its large FOV of about $10' \times 10'$ within a pointing opportunity.

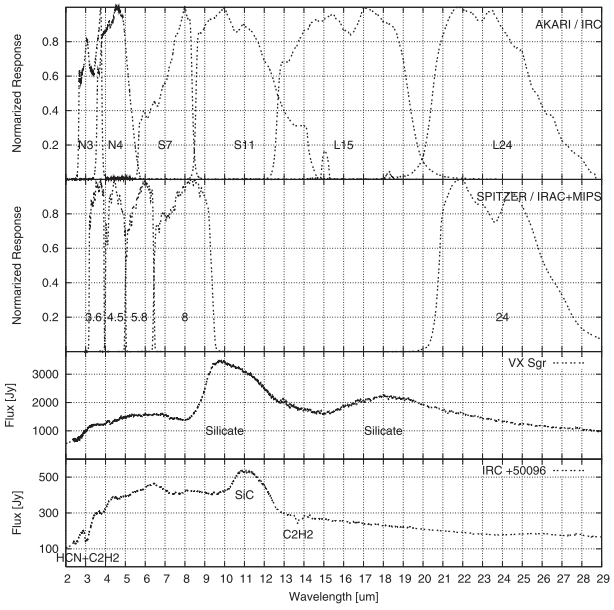

Fig. 2. Normalized spectral response function of AKARI IRC bands and Spitzer IRAC and MIPS bands. As references, the ISO SWS spectra of two representative galactic AGB stars (VX Sgr as O-rich AGB and IRC +50096 as C-rich AGB) with circumstellar dust features are shown.

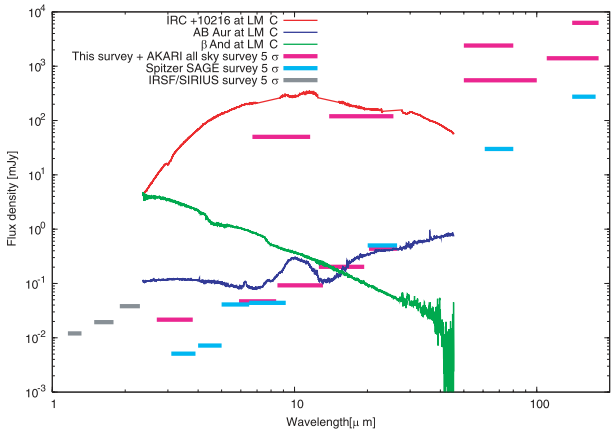

Fig. 3. Graphic representation of the 5σ detection limits of the AKARI LMC survey and the All-Sky Survey (magenta). For a comparison, the 5σ detection limits of the Spitzer SAGE survey and the IRSF/SIRIUS survey are also shown (cyan and gray, respectively). Some ISO SWS spectra (Sloan et al. 2003) of famous galactic stars are scaled to fit the distance to the LMC, and are included in the figure, as examples of Herbig Ae/Be stars (AB Aur), red giants with luminosities below the tip of the first red-giant branch (β And), and dusty red giants (IRC +10216) in the LMC.

These features make AKARI IRC unique and complementary to IRAC and MIPS on the SST. Refer to Onaka et al. (2007) for instrumental details and the imaging performance of the IRC. General information on the IRC spectroscopic mode, particularly on slit-less spectroscopy, is given in Ohyama et al. (2007).

3. Scientific Objectives

Interstellar matter in a galaxy is thought to evolve through various processes. Stars are born in interstellar clouds by accreting of the interstellar matter, and then appear as young stellar objects (YSOs), such as T Tauri stars or Herbig Ae/Be stars. Low- and intermediate-mass stars evolve into white dwarfs after spending most of their lives in the main sequence. During the course of their evolution to white dwarfs, they lose mass through the so-called mass-loss process, and supply dust grains and gas to interstellar space. High-mass stars end their lives as supernovae, and enrich the interstellar medium with a large amount of nuclear synthesized elements. They can also trigger the formation of next-generation stars through their strong UV photons and stellar winds (Hosokawa & Inutsuka 2006; Koo et al. 2008). Interstellar grains play an important role in every aspect of these interstellar processes, including star-formation. All of these phenomena can be studied most effectively in the infrared. The Spitzer SAGE project (Meixner et al. 2006) has provided IRAC (3.5, 4.5, 5.8, and 8.0 μm) and MIPS (24, 70, and 160 μm) images for a wide area ($7^\circ \times 7^\circ$) of the LMC. Adding to the SAGE observation, the complementary AKARI IRC (3.2, 7.0, 9.0, 11.0, 15.0, and 18.0 μm) and FIS (65, 90, 140, and 160 μm) observations of the LMC will provide an opportunity to make a thorough study of these material circulation processes and the local star-formation history of the LMC on a galactic scale, owing to its wide spectral coverage and high sensitivities together with sufficient spatial resolution.

Figure 3 is a diagrammatic representation of the 5σ detection limits of our survey, Spitzer SAGE survey, and the IRSF/SIRIUS near-infrared survey. The 5σ detection limits of our survey are calculated by scaling the 10σ detection limits given in table 1 (see subsubsection 5.4.1). We take the 5σ detection limits for the SAGE survey from the "SAGE Data Description: Delivery 1".[1] The detection limits are expected to be further improved in the final catalog deliveries (Meixner et al. 2006). It is clear that the detection limits of our survey are comparable to that of the Spitzer SAGE survey. The ISO SWS spectra of galactic famous stars of known distances [the distances were taken from Crosas & Menten (1997) for IRC +10216, and Perryman et al. (1997) for others] were included for illustrative purposes after scaling their fluxes at the distance of the LMC. We assumed a distance modulus of 18.5 mag to the LMC. The figure indicates that all red giants above the tip of the first red giant branch, and a large fraction of Herbig Ae/Be stars in the LMC were detected in our survey.

3.1. *Star-Formation and Young Stars*

The LMC contains a class of so-called populous clusters (e.g., Kumai et al. 1993) that have no galactic counterpart. They have masses intermediate between galactic globular clusters and open clusters. The characteristic environments in the LMC, such as low mean metallicity (about 1/4 of the solar vicinity), low dust-to-gas ratio (about 1/4 of Milky Way: Koornneef 1982) and strong ultraviolet interstellar radiation (e.g., Cox & Spaans 2006), may play a key role in the star-formation process of populous clusters (Fukui 2005). Detailed studies of star formation in the LMC will provide insights into

[1] ⟨http://sage.stsci.edu/index.php⟩.

Table 1. Survey properties.

Properties	IRC bands					
	NP	*N3*	*S7*	*S11*	*L15*	*L24*
Channel	NIR	NIR	MIRS	MIRS	MIRL	MIRL
Bandpass [μm]	1.8–5.5	2.7–3.8	5.9–8.4	8.5–13.1	12.6–19.4	20.3–26.5
Reference wavelength [μm]	—	3.2	7.0	11.0	15.0	24.0
Pixel field of view [$''$/pixel]	—	1.446	2.340	2.340	2.384	2.384
Dispersion [μm/pixel]	0.06 at 3.5 μm	—	—	—	—	—
Exposure time: long exposure* [s]	133.2432	133.2432	147.2688	147.2688	147.2688	147.2688
Exposure time: short exposure* [s]	14.0256	14.0256	1.7532	1.7532	1.7532	1.7532
10 σ detection limit† [mJy]	—	0.086	0.188	0.369	0.811	1.744
10 σ detection limit† [mag]	—	16.50	14.00	12.54	10.74	9.16
Saturation limit†,‡ [mJy]	12500 at 3.5 μm	250	1800	1800	2500	23000
Saturation limit†,‡ [mag]	3.6 at 3.5 μm	7.8	4.0	3.3	2.0	−1.1
Zero magnitude flux§ [Jy]	—	343.34	74.956	38.258	16.034	8.0459
Number of detected sources	—	$> 5.9 \times 10^5$	$> 8.8 \times 10^4$	$> 6.4 \times 10^4$	$> 2.8 \times 10^4$	$> 1.5 \times 10^4$

* These are the most common values. Total exposure time per pixel can be different from coadded images to images, because some data badly damaged by cosmic-ray and/or hitting of charged particles are discarded.
† For point sources.
‡ Numbers are taken from ASTRO-F Observer's Manual version 3.2.[2]
§ Tanabé et al. (2008).

these processes. The IRAS survey has detected protostars in the LMC only brighter than 10^4–$10^5\,L_\odot$ (e.g., van Loon et al. 2005). Although only the brightest end of the YSOs in the LMC can be detected by the IRC (see the detection limits provided in table 1), the IRC imaging data provide a valuable dataset to investigate the nature of such objects from the spectral energy distribution from near- to mid-infrared as well as the water ice feature at 3 μm and/or silicate absorption at 10 and 20 μm. AKARI observations of the LMC enable us to probe the luminosity function of protostars down to about $10\,L_\odot$.

The detection limits of IRC bands are not deep enough to detect T Tauri stars in the LMC. However, the IRC observations can nearly completely detect young stars of intermediate mass (Herbig Ae/Be) as well as classical Be stars. It is difficult to separate Herbig Ae/Be stars from classical Be stars and another kind of young stars with different masses and ages, based on near-infrared data alone. Mid-infrared data provided by the IRC make clear identification of these objects. AKARI IRC observations are able to provide the initial mass function of objects later than the Class 1 phase for $M > 2$–$3\,M_\odot$, except for dense clusters, where the source confusion limits the detection. They allow us to compare the spatial distribution of YSOs with that of CO clouds in a statistical way, and to investigate the star-formation history in the LMC. Particularly interesting is the search for embedded star clusters in "cluster-less" giant molecular clouds (GMCs), such as N 159 S (Bolatto et al. 2000) and investigation of whether or not these cluster-less GMCs are really not associated with star clusters. The 5-band IRC observations together with the 4-band FIS All-Sky Survey data allow us to distinguish these YSOs unambiguously and to study the nature of detected objects in detail.

[2] ASTRO-F Observer's Manual, version 3.2, 2005 November 29, ⟨http://www.ir.isas.jaxa.jp/ASTRO-F/Observation/ObsMan/afobsman32.pdf⟩.

3.2. *Evolved Stars*

Stars of low- to intermediate-mass (stars with main-sequence masses, $M_{\rm ms}$, of about 0.8–8 $M_\odot$) eventually evolve into white dwarfs. The mass $M_{\rm wd}$ distribution of white dwarfs peaks at around $0.6\,M_\odot$ (e.g., Kepler et al. 2007). Therefore, the difference, $\Delta M = (M_{\rm ms} - M_{\rm wd})$, should be lost during their life in the mass-loss process, which enriches gas and dust in the interstellar medium. It is observationally known that the maximum mass-loss rate is attained at the latest stage of their Asymptotic Giant Branch (AGB) evolutionary phase, where stellar pulsation is usually associated. However, the onset and evolution of the mass-loss process and its relation to pulsation are not yet completely understood.

As described above, the LMC has a number of young clusters, which also provide a unique place to study the late evolutional stage of intermediate-mass stars. Star clusters of intermediate ages still contain a number of AGB stars that are losing mass. Since their ages and masses are well determined, the study of mass-losing AGB stars in clusters can elucidate the mass-loss process for stars with given ages and masses quantitatively for the first time.

Blum et al. (2006) used the Spitzer SAGE survey epoch 1 catalog to discuss and identify evolved stars in the infrared color–magnitude diagrams. Ita et al. (2004a,b) studied OGLE variables in Magellanic Clouds (Udalski et al. 1997; Żebruń et al. 2001). They detected most of the optical variable stars in the central parts of the Large and Small Magellanic Clouds. The association of the IRC data with these variability catalogs enables us to investigate the mass-loss phenomena in terms of the pulsation activity directly. The IRC observations can detect all mass-losing AGB stars in the LMC. It should be emphasized that the IRC bands *S11*, *L15*, and *L24* are particularly important to determine the chemistry of the envelope (O-rich or C-rich) and the mass-loss rate accurately because of the presence of the

silicate bands at 10 μm and 18 μm and a silicon carbide band at 11.3 μm.

3.3. Supernova Remnants

Supernovae (SNe) are believed to be a major source of interstellar dust, since the expected supply rate from late-type stars is too short to balance with the dust destruction rate in interstellar space (Jones et al. 1994, 1996). The role of dust production in SNe is crucial to understand the circulation and evolution of materials in the interstellar medium (Dwek 1998). However, to date, no clear observational evidence has been given for the large production of dust grains from SNe (Meikle et al. 2007). The condensation efficiency could be either very low (Clayton et al. 2001) or moderate (Todini & Ferrara 2001). A study of Cas A SNR by Spitzer clearly demonstrates the observational difficulty of dust grains associated with SNRs in our Galaxy (Krause et al. 2004). SNRs in the Galaxy are easily confused by material on the line of sight, because most of them are located on the galactic plane. In this regard, the LMC provides an ideal opportunity to study material ejected in SNRs without suffering from serious confusion problems. Recent studies of SNRs in the LMC with Spitzer and AKARI provide significant information on the origin of the IR emission in SNRs and the interstellar dust lifecycle in terms of dust formation by SNe and dust distraction by SNR blast waves (e.g., Borkowski et al. 2006; B. Williams et al. 2006; R. Williams et al. 2006; Rho et al. 2008; Seok et al. 2008).

The interaction of SNRs with their surroundings is also an important phenomenon, providing opportunities for studying strong shocks and sometimes triggered star-formation (Koo et al. 2007, 2008). However, any observational study of the interaction is also hampered by confusion for galactic SNRs. There are more than 40 SNRs known in the LMC (Filipovic et al. 1998; Haberl & Petsch 1999), and only 10 of them have been detected by IRAS. SNRs appear to be very patchy in the infrared (Douvion et al. 2001), and their spectral energy distribution indicates their multi-temperature nature. They also have many emission lines, which could affect broad-band photometry. Strong emission lines expected in the MIR are [Ar II] 7.0 μm, [Ne II] 12.8 μm, [Ne III] 15.6 μm, [Fe II] 17.9 μm, [Fe II] 24.5, 26.0 μm, and [Si II] 34.8 μm (e.g., Arendt et al. 1999; Temim et al. 2006; Rho et al. 2008). Dust grains in SNRs may be transiently heated by high-energy electron hits, which result in a wide dust temperature distribution (Dwek 1986). A peculiar band may also be present in the MIR (Arendt et al. 1999), which might be associated with dust grains formed in the SNR (Chan & Onaka 2000; Onaka et al. 2008). Therefore, multi-band photometry spanning over a wide spectral range with sufficient spatial resolution is crucial to study the nature of the infrared emission from SNRs, and could confirm the physical association of the emission with SNRs.

3.4. Interstellar Matter

Diffuse infrared emission from interstellar dust consists of several components: thermal emission in the FIR from submicron size grains, excess continuum emission in 15.80 μm, and unidentified infrared (UIR) emission bands arising from aromatic materials (Onaka 2000). Each component should play a significant role in the interstellar process and their relative variations in abundance should provide valuable information on the physical conditions of the interstellar medium. However, little has been known concerning the formation, evolution (processing), and destruction of each dust component. A study of the UIR bands in our Galaxy has suggested possible variations in the relative abundance to the submicron grains as well as in the band appearance with the Galacto-centric distance for the first time (Sakon et al. 2004). Observations of the galactic plane pick up diffuse emissions from every component on the line of sight, and it is impossible to separate out the emission from a particular region. The LMC again provides an ideal place to study the diffuse infrared emission from dust grains in several different environments compared to our Galaxy because of its nearly face-on geometry. It has been suggested that the nature of the infrared emission from the LMC is different from our Galaxy (Aguirre et al. 2003), which may be related to the low metallicity of the LMC. A recent study of IRAS data has indicated that the color of the IRAS 12 μm to 25 μm intensities seems to be high in CO clouds without young star clusters, whereas it is low in regions with YSOs (Sakon et al. 2005). There is also an indication that the 12 μm-to-100 μm ratio is different inside supergiant shells (Kim et al. 1998), which is also related to the star-formation activity (Yamaguchi et al. 2001). Since the IRAS 12 μm band intensity includes both the UIR and the MIR excess emissions, it is important to separate the contribution from each component and to compare it directly to the FIR component. The IRC *S7* filter is most sensitive to the 6.2 and 7.7 μm UIR bands, whereas the *S11* band can probe the UIR 11.2 μm band. The *S7*-to-*S11* band ratio together with the MIR and FIR All-Sky Survey data can investigate variations in the relative band strength efficiently. The *L15* and *L24* band data determine the contribution and spectral profile of the MIR excess component unaffected by the UIR bands.

4. Observations

4.1. IRC Astronomical Observing Template and Pointing Observation Sequence

To cover a wide range of the spectral energy distribution of a celestial body, we use the AKARI IRC AOT02 observing template with a special option prepared only for the LMC survey. The AOT02 with the special option yields not only imaging data at 3 μm (*N3*), 7 μm (*S7*), 11 μm (*S11*), 15 μm (*L15*), and 24 μm (*L24*), but also low resolution ($\lambda/\Delta\lambda \sim 20$) 2.5–5 μm (NP) spectral data at three dithered sky positions in a pointing opportunity. Figure 4 shows an example of the NP spectroscopic data taken in our survey. The reduced spectrum of a red source indicated in the box is also shown in the figure. Discussions on spectroscopic data will be given in a future paper.

As described in the IRC data user's manual (R. Lorente et al. 2007)[3] the IRC observation produces short- and long-exposure data together. The long-to-short exposure time ratios in each channel are 9.5, 28, and 28 for NIR, MIRS, and MIRL, respectively. It enhances the dynamic range by combining photometric results of the two different exposure-time data. In this

[3] AKARI IRC Data User's Manual ver. 1.3 ⟨http://www.ir.isas.jaxa.jp/AKARI/Observation/#IDUM⟩.

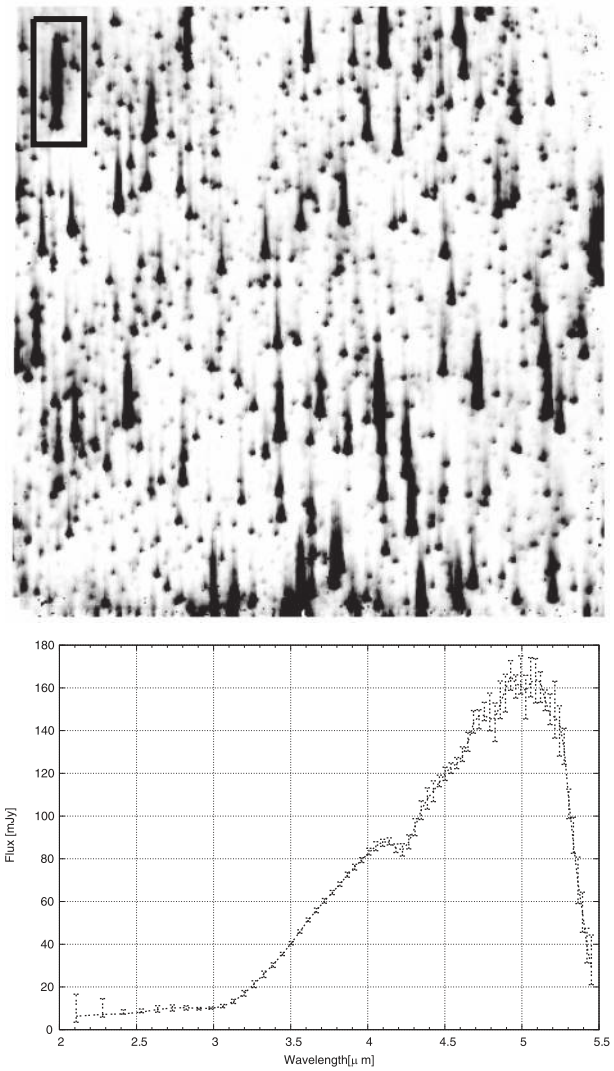

Fig. 4. Sample image of NP slit-less spectroscopy data taken in our survey and a reduced NP spectrum of a source indicated in the box.

paper, we use the combined data of long- and short-exposure for *N3*, but only use long-exposure data for MIRS and MIRL.

4.2. Mapping Strategy

Due to the focal-plane layout of AKARI, the NIR and MIRS channels share the same field of view (i.e., they observe the same sky position), but the MIRL channel observes a different sky position, which is offset by 25′ from the NIR/MIRS center in the direction perpendicular to the AKARI's orbit. AKARI is in a Sun-synchronous polar orbit at 700 km attitude along the twilight zone, and its orbit is approximately parallel to the ecliptic meridian lines with approximately 4.′1 spacing at the ecliptic plane between successive orbits. We used this feature to map the LMC effectively. Each of the IRC channels has a field of view of $10' \times 10'$, and adjacent fields are designed to overlap by $\sim 1.'5$. Since AKARI follows the Earth's yearly round, the telescope points at the same celestial position every six months, but the direction of the satellite movement relative to the position is rotated by 180°. Thus, the position of the MIRL channel relative to the NIR and MIRS channels is also rotated by 180° in projection on the sky. Therefore, we divide the observing area into several parts to maximize the observing efficiency to map a large part of the LMC with all three channels of the IRC. Observations were carried out in three separate seasons, from 2006 May 6 to 2006 June 8, from 2006 October 2 to 2006 December 31, and from 2007 March 24 to 2007 July 2. Over 600 pointing observations were devoted for this project, yielding about a 10 deg^2 imaging and spectroscopic map of the main part of the LMC.

5. Data Reduction

5.1. Pipeline Processing

Raw imaging data were processed with the IRC imaging toolkit, version 20071017 (see IRC Data User's Manual[2] for details). In a pointing observation using IRC, one short-exposure and three long-exposure dark data are taken at the beginning (pre-dark) and the end of the operation for all of the three IRC channels. We made long-exposure dark images for MIRS and MIRL channels by averaging over three long exposure dark data. We refer to these averaged pre-dark images as selfdark. We subtracted selfdarks from MIRS and MIRL long-exposure images and the pipeline default super-dark from the others.

As described above, we use the AKARI IRC AOT02 observing template that produces data at three different sky positions in a pointed observation. The data in each band are spatially aligned and then coadded by taking their median to eliminate any array anomalies, such as bad, dead, or hot pixels, cosmic rays, and so on. The resultant coadded images have pixel sizes of 1.″446 pixel^{-1}, 2.″340 pixel^{-1} and 2.″384 pixel^{-1} for NIR, MIRS, and MIRL images, respectively.

5.2. Astrometry

After the coaddition process, we calculate the coordinate transform matrix that relates the image pixel coordinates to the sky coordinates by matching detected point sources with the Two Micron All Sky Survey (2MASS: Skrutskie et al. 2006) catalog. We use at least five matched point sources for a calculation. If matching with the 2MASS catalog is unsuccessful (such cases usually occur in *L15* and *L24* images), we then use the SAGE point source catalog (Meixner et al. 2006) as a positional reference. The root-mean-squares of the residuals between the input 2MASS/SAGE catalog coordinates and the fitted coordinates are smaller than 1.″2, 2.″6, and 2.″9, for NIR, MIRS, and MIRL images, respectively. The coordinates of the AKARI sources should be accurate to that extent relative to the 2MASS and SAGE catalog coordinates.

5.3. Photometry

Photometry is carried out for each coadded image independently. To derive calibrated fluxes for each detected source, point spread function (PSF) fitting photometry was performed on the coadded images with the IRAF[4] package DAOPHOT.

[4] IRAF is distributed by the US National Optical Astronomy Observatories, which are operated by the Association of Universities for Research in Astronomy, Inc., under cooperative agreement with the National Science Foundation.

We developed PSF fitting photometry software, which is similar to the one that the Spitzer GLIMPSE[5] (Benjamin et al. 2003) team uses. Our photometric process involves the following steps:

1. Source extractor (Bertin & Arnouts 1996) is used for each coadded image to extract sources whose fluxes are at least $3\,\sigma$ above the background. The saturated sources should not be extracted, since their central pixels are already masked by the IRC imaging toolkit. Even if they are detected by the source extractor, the PSF fitting does not work well for them, and they are not included in the following discussions.
2. Aperture photometry is performed on all of the sources found in step 1, using the task PHOT with aperture radii of 10.0 and 7.5 pixels for NIR and MIRS/MIRL images, respectively. We use the same aperture radii as have been used in the standard star flux calibration (Tanabé et al. 2008), and the aperture corrections are not applied. The resultant arbitrary fluxes are converted into the physical units by using the IRC flux calibration constants version 20071112. Then the calibrated fluxes are converted into the magnitudes of the IRC-Vega system by using the zero magnitude fluxes listed in table 1. The offsets between the arbitrary and the calibrated magnitudes are constants.
3. Several point sources with moderate flux (i.e., with a good signal-to-noise ratio and unsaturated) and without other sources within 7 pixels are selected from the results of step 2. At least 8 such "good" stars are selected in the NIR/MIRS (i.e., *N3*, *N4*, *S7*, and *S11*) images, and more than 5 good stars in the MIRL (i.e., *L15* and *L24*) images. They are used for the aperture correction to the PSF fitting photometry in the following process.
4. Since the shapes of the PSFs measurably vary from pointing to pointing in NIR images, possibly due to jitters in the satellite pointing, the selected good stars in step 3 are used to construct a model PSF for each image. We use DAOPHOT to choose the best fitting function by trying several different types of fitting functions. In MIRS/MIRL images, we use a "grand-PSF" for each band, which was built in advance. These grand-PSFs were made from "good" stars free from diffuse emission, carefully chosen by eye from hundreds of images taken in the AKARI/IRC LMC survey data and other related ones.
5. The PSF fitting photometry is performed on all of the sources found in the coadded images using ALLSTAR. The PSF does not vary appreciably over the field of view. Hence, a constant PSF is assumed over an image. This PSF fitting operation is iterated, in just the same way as does the GLIMPSE team.
6. An aperture correction is applied to the fit magnitudes by comparing them with the aperture magnitudes of good stars, which are selected in step 3. Then, the offset value obtained in step 2 is added to the aperture-corrected fit magnitudes to derive calibrated fit magnitudes.

[5] Visit ⟨http://www.astro.wisc.edu/glimpse/⟩, and see a document "Description of Point Source Photometry Steps Used by GLIMPSE", written by Dr. Brian L. Babler.

As indicated above, we use the zero magnitude fluxes (Tanabé et al. 2008) to convert the photometric fluxes into the Vega magnitudes. These zero-magnitude fluxes are tabulated in table 1. It should be noted that the IRC absolute flux calibration assumes a spectral energy distribution (SED) of $f_\lambda \propto \lambda^{-1}$ or $f_\nu \propto \nu^{-1}$. Note that throughout this paper, we do not apply color corrections to the calibrated fluxes and magnitudes. No dereddening are applied either.

5.4. *Compilation of a Preliminary Catalog*

We carried out photometry on each coadded image, as outlined in the previous section. It produced photometric catalogs for each band for individual images. At first, the catalogs for individual IRC imaging bands (i.e., *N3*, *S7*, *S11*, *L15*, and *L24*) were made. Because of the field overlap, there should be substantial multiple entries of a single source in the catalogs. We eliminated such multiple entries based on the spatial proximity ($|\Delta r| \leq 1\farcs5$). We adopted the one with a better S/N and discarded the other(s). We used both long- and short-exposure data of *N3*, and merged them using a positional tolerance of $1\farcs5$. If a source was detected in both short and long-exposure data, we adopted the one with a better S/N, and discarded the other. Then, two corresponding band catalogs were merged to make individual IRC channel catalogs. The, *S7* and *S11* (*L15* and *L24*) catalogs were merged using a positional tolerance of $1\farcs5$ ($1\farcs5$) to make a MIRS (MIRL) channel catalog. For the matched sources, their coordinates were recalculated by taking an average of the coordinates of each band. In rare cases that more than two sources are present within the tolerance radius, the closest one was always adopted and the others were listed as solitary sources. The resultant individual channel catalogs were further merged to make a grand catalog using a positional tolerance of $1\farcs5$.

5.4.1. *Detection limits and completeness*

The distributions of the photometric uncertainty versus the magnitude in the IRC bands are shown in figure 5. The photometric uncertainty includes errors in the fitted magnitude calculated by IRAF/ALLSTAR, in the aperture correction factor, and also in the ADU-to-Jy conversion factor. The horizontal dashed lines show the signal-to-noise ratio (S/N) of 10, and the vertical solid lines show the $10\,\sigma$ detection limits, which are defined as the faintest magnitudes at which the mode of the photometric uncertainties of the sources in 0.02 mag bins exceed $10\,\sigma$, except for the *N3* data. In calculating the $10\,\sigma$ detection limit for the *N3* data, we used only data detected in long exposure images, and took a mean of the photometric uncertainties in 0.02 mag bins instead of taking a mode of them. Visual inspections showed that sources can be detected only in short exposure images, and this is why there is a sequence around 15 mag in the *N3* error plot. There seems to be several causes to explain this. For example, not a small number of long-exposure images are damaged by column pull-downs caused by saturated stars, and sources in such polluted columns are not detected in the long-exposure images. The estimated $10\,\sigma$ detection limits are 16.50, 14.00, 12.54, 10.74, and 9.16 in *N3*, *S7*, *S11*, *L15*, and *L24*, respectively. These detection limits are comparable to that of the Spitzer SAGE survey (see figure 3).

The magnitude distributions of the sources in the preliminary

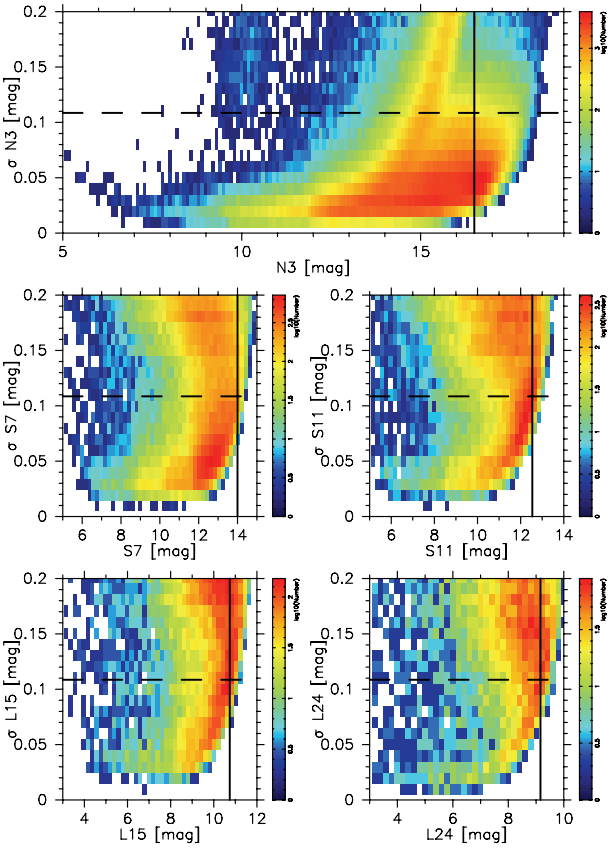

Fig. 5. Photometric uncertainties as a function of the magnitude at each IRC band. The sizes of the bins are 0.1 mag × 0.01 mag for *N3*, and 0.2 mag × 0.01 mag for *S7*, *S11*, *L15*, and *L24*. The dashed lines show 10 σ errors, and the solid lines indicate the 10 σ detection limits: 16.50, 14.00, 12.54, 10.74, and 9.16 mag in *N3*, *S7*, *S11*, *L15*, and *L24*, respectively.

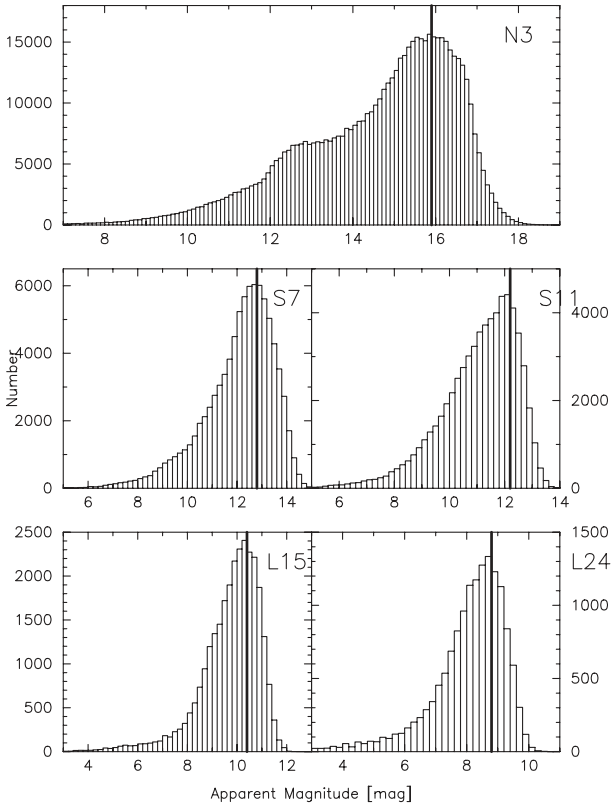

Fig. 6. Magnitude distribution of the sources in the AKARI LMC survey catalog. The sizes of the bins are 0.1 mag for *N3*, and 0.2 mag for *S7*, *S11*, *L15*, and *L24*. The solid lines show the peak of the source count histograms, below which the photometry is incomplete: 15.9, 12.8, 12.2, 10.4, and 8.8 mag in *N3*, *S7*, *S11*, *L15*, and *L24*, respectively.

catalog are shown in figure 6. The sizes of the bins are 0.1 mag for *N3* and 0.2 mag for *S7*, *S11*, *L15*, and *L24*. The vertical solid lines show peak magnitudes, below which photometry is incomplete. The peak magnitudes are 15.9, 12.8, 12.2, 10.4, and 8.8 mag in *N3*, *S7*, *S11*, *L15*, and *L24*, respectively.

The 10 σ detection limits for point sources and source counts in each IRC band are summarized in table 1 together with other properties of our survey.

5.4.2. Cross-identifications with the existing point source catalogs

We cross-identified our catalog with the following existing catalogs using a positional tolerance of 1.″5, and use the result for discussion in the rest of the paper:

- The Magellanic Clouds Photometric Survey catalog (Zaritsky et al. 2004): It lists *U*, *B*, *V*, and *I* stellar photometry of the central 64 deg^2 area of the LMC.
- The IRSF Magellanic Clouds Point Source Catalog (Kato et al. 2007): The IRSF catalog lists JHK_s photometry of over 1.4×10^7 sources in the central 40 deg^2 area of the LMC. Compared to the contemporary DENIS (Cioni et al. 2000a) and 2MASS (Skrutskie et al. 2006) catalogs, the IRSF catalog is more than two mag deeper at the K_s-band and about four-times finer in spatial resolution.
- The Spitzer SAGE catalog (Meixner et al. 2006): It lists near- to far-infrared photometry of sources in the central 49 deg^2 area of the LMC.

The observed regions of the above existing catalogs are indicated in figure 1. The figure shows that a part of the AKARI IRC survey region is outside the bounds of the IRSF/SIRIUS survey area. We do not use the AKARI sources located outside the IRSF/SIRIUS area in the following discussions. Throughout this paper, the numbers bracketed by *[ ]* designate data of the SAGE catalog; for example, *[3.6]* indicates photometry in the IRAC 3.6 μm band.

5.4.3. Comparison to the Spitzer SAGE survey catalog

Although the bandpasses of the AKARI IRC and the Spitzer IRAC/MIPS bands are different, a comparison of closely matched bands is useful to test the calibration of the AKARI IRC data. We compared the IRC *N3*, *S7*, *L24* photometries in our catalog with the corresponding 3.6, 8.0, and 24 μm fluxes of the sources in the Spitzer SAGE catalog. Note that both of the IRC and IRAC absolute flux calibrations assume a SED of $f_\nu \propto \nu^{-1}$, but MIPS flux scale assumes a source spectrum of a 10000 K blackbody (MIPS Data Handbook).[6]

[6] MIPS Data Handbook, version 3.3, ⟨http://ssc.spitzer.caltech.edu/mips/dh/mipsdatahandbook3.3.pdf⟩.

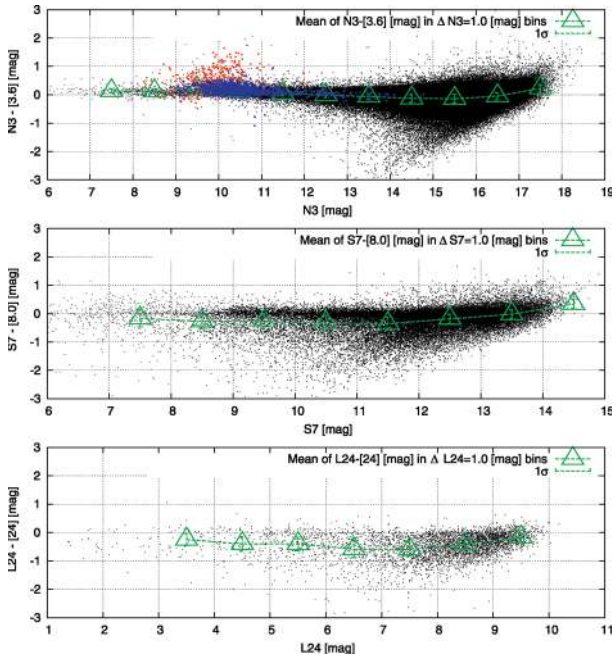

Fig. 7. Comparison between the AKARI LMC survey and the Spitzer SAGE catalog using closely matched passbands (top panel: *N3* vs. *[3.6]*, middle panel: *S7* vs. *[8.0]*, bottom panel: *L24* vs. *[24]*). In the *N3* vs. *[3.6]* panel, the spectroscopically identified carbon stars (optical prism survey, Kontizas et al. 2001) are indicated by blue dots, and photometrically selected (see text for selection conditions) carbon-rich AGB candidates are shown by red dots.

Therefore we converted the MIPS scale into the IRC/IRAC one by adding −0.043 mag (Bolatto et al. 2007) to the MIPS 24 catalog magnitudes to make a direct comparison between the *L24* and MIPS 24 μm photometries. The distributions of the magnitude differences between the IRC and IRAC/MIPS fluxes as a function of the corresponding IRC magnitudes are shown in figure 7. The triangles show the mean of the residual magnitudes in the corresponding 1 mag bin, and the error bars show their $1\,\sigma$ standard deviations. Taking account of the differences in the bandpass, the AKARI IRC and IRAC/MIPS photometries appear to be consistent with each other. Quantitatively, they are in agreement within 9, 10, and 11% in *N3* vs. *[3.6]*, *S7* vs. *[8.0]*, and *L24* vs. *[24]* comparisons, respectively, using sources with S/N $> 10\,\sigma$ and after subtracting systematic offsets.

In a comparison between *N3* and *[3.6]* photometries, we find an interesting feature. It is seen that a group of bright sources (sources with $9 <$ *N3* [mag] < 11) deviate from the overall trend. To explain this deviation, we cross-identified our sources with spectroscopically identified carbon stars (Kontizas et al. 2001), which are shown by blue dots. We photometrically selected dusty carbon-rich AGB candidates that could not be identified in an optical survey based on the following conditions:

- $(J - K_{\rm s}) > 2.0$
- $K_{\rm s} < (4/3) \times [(J - K_{\rm s}) - 2.0] + 12.0$

These sources are indicated by red dots. The J and $K_{\rm s}$ fluxes are obtained by cross-identifying the IRC catalog with the IRSF/SIRIUS LMC near-infrared catalog (Kato et al. 2007, see next section). It is true that the above conditions may include some dusty O-rich AGB stars, but such stars are small in number compared to the carbon-rich AGB stars. It is clearly seen that red dots are the sources that show the deviation in the diagram. The deviation should be attributed to the fact that the passband of the IRC *N3* band is slightly bluer than that of the IRAC 3.6 μm, and it is more sensitive to the 3.1 μm HCN + C_2H_2 absorption feature, which is usually seen in carbon-rich AGB stars (e.g., Yamamura & de Jong 2000). The *N3* data, thus, enable us to select sources with carbon-rich circumstellar chemistry on the basis of their colors.

6. General Analysis Using the AKARI LMC Survey Photometric Catalog

6.1. Color–Color Diagram

6.1.1. Convolution of ISO SWS spectra

With an aim to help to interpret what types of sources are detected by the AKARI survey, we take fully calibrated ISO SWS spectra data from the available on-line database[7] (Sloan et al. 2003). We then estimate their fluxes in the AKARI IRC system by convolving the ISO SWS spectra with the response curves of the IRC bands using the following equation:

$$f_{\lambda_i}^{\rm reference} = \frac{\int \frac{R_i(\lambda)}{h\nu} f_\lambda(\lambda) d\lambda}{\int \left(\frac{\lambda_i}{\lambda}\right) \frac{R_i(\lambda)}{h\nu} d\lambda}, \quad (1)$$

where the suffix i denotes IRC bands, λ_i represents the reference wavelengths of each IRC band tabulated in table 1, and $R_i(\lambda)$ indicates the spectral responses of each band. The calculated fluxes are further converted into the Vega-magnitudes. Note that the calculated magnitudes are in the IRC system [substituting $\lambda f_\lambda(\lambda) = {\rm constant}$ to equation (1) gives $\lambda_i f_{\lambda_i}^{\rm reference}$], which can be directly compared with the catalog values.

We divide ISO SWS sources into 10 main groups, based on table 6 in Kraemer et al. (2002). Sources that are classified as "uncertain classification" and "very uncertain classification" in Kraemer et al. (2002) are excluded in the following discussions. Table 2 summarizes how we group the ISO SWS sources.

6.1.2. (S11 − L15) vs. (N3 − S11) diagram

Figure 8 shows color–color diagrams of AKARI sources (upper panel) and ISO SWS sources (lower panel) using colors of (*S11* − *L15*) and (*N3* − *S11*). In the AKARI diagram, only stars with S/N > 5 in all employed three bands are included. The numbers of sources in each 0.05×0.05 mag^2 bin are counted and the fiducial color is applied according to their number densities (see the annotated color wedge). The solid gray line in the lower panel shows the blackbody locus with the temperature ranging from 400 to 10000 K in the IRC system.

It is obvious that a wide variety of sources are detected in our survey. Comparing the two diagrams, we can statistically separate various types of objects. Two distinct main groups appear

[7] ⟨http://isc.astro.cornell.edu/~sloan/library/swsatlas/atlas.html⟩.

Table 2. Source classification.

Grouped as	Classification in Kraemer et al. (2002)	Marks in figure 8
Naked stars without salient molecular bands	1.N	+
Naked stars with C-rich molecular bands	1.NC	×
Naked stars with O-rich molecular bands	1.NO	●
Naked stars with emission lines (Be stars)	1.NE	□
Red giants with C-rich dust	2.CE, 3.CE, 3.CR, 4.CR	●
Red giants with O-rich dust	2.SE, 3.SB, 3.SE	×
Wolf–Rayet and R CrB	3.W	+
C-rich proto planetary nebulae (PPNe)	4.CN, 4.CT	●
Planetary nebulae (PNe)	4.PN, 4.PU, 5.PN	+
OH/IR,PPNe,PNe,YSOs*	4.SA, 4.SB, 4.SE, 4.SEC, 4.U/SC, 5.E, 5.SA, 5.SE, 5.U	△

* Young stellar objects, such as T Tau stars and Herbig Ae/Be stars.

in the AKARI diagram: one centered around (*S11* − *L15*, *N3* − *S11*) of (0.1, 1.0), and the other centered around (1.0, 4.0).

The former group includes two peaks, one centered around (0.2, 0.2), and the other centered around (0.25, 0.8). Based on a comparison with the ISO SWS classification, the sources in the first peak are stars without circmstellar dust, and the second peak is associated with red giants having circmstellar dust emission. ISO SWS spectra indicate that red giants with O-rich dust as well as C-rich dust may once become blue in the (*S11* − *L15*) color, and then turn red again in the course of their evolution. This can be explained by a change in the strength of silicate or silicon carbide dust features in the *S11* band relative to the *L15* flux.

According to the ISO SWS spectra, the red group may contain various types of objects, such as PPNe, PNe, OH/IR stars, and YSOs. Also, the background galaxies may have similar colors (see the following), which makes the classification more difficult. The NP spectroscopic data, and follow-up spectroscopic observations are needed to make clear classifications of these objects.

6.2. *Color–Magnitude Diagrams*

An advantage of studying sources in the LMC is that we can build color–magnitude diagrams (CMD) and estimate their absolute magnitudes by adding the distance modulus, which is reasonably well-known (e.g., Feast & Walker 1987). Based on the Spitzer SAGE catalog, Meixner et al. (2006) and Blum et al. (2006) presented infrared color–magnitude diagrams of LMC sources. Here, we add *S11* and *L15* data, which are unique to the AKARI survey. We used intriguing combinations of the IRC, IRAC&MIPS, and IRFS/SIRIUS bands; the results are shown in figure 9. The units of the vertical axes are the apparent magnitudes. It can be scaled to the absolute magnitude by subtracting the distance modulus. The corresponding wavebands for the vertical axes are indicated at the top of each panel. The employed colors for the horizontal axes are indicated at the bottom of each panel. All of the color–magnitude planes are binned by $0.1 \times 0.1\,\mathrm{mag}^2$ to calculate the number of sources in each bin, and the fiducial color is given according to the number density levels on a logarithmic scale (see the wedge at the bottom). Other than the trends pointed out in Meixner et al. (2006) and Blum et al. (2006), new features are seen in our figure, primarily due to the addition of *S11* band data.

6.2.1. *New sequence for faint red giants with circumstellar dust*

Ramdani and Jorissen (2001) showed that the ratio of the ISO 11.5 μm to DENIS K_s 2 μm flux density is a good indicator of dust mass-loss from red giants. The (K_s − *S11*) vs. K_s panel indicates which red giants show circumstellar dust emission. It is clear that excess in *S11* (K_s − *S11* > 0.5) is seen not only among the sources brighter than the tip of the first red giant branch (TRGB, $K_\mathrm{s} \sim 12.5$ mag: Cioni et al. 2000b), but also among the sources below the TRGB. Since the brighter sources exceed the K_s luminosity of the TRGB, they should be an intermediate-age population and/or metal-rich old population AGB stars. On the other hand, an interpretation of the fainter sources is difficult. They can be metal-poor and old AGB stars that do not exceed the TRGB luminosity, or red giants on the first red-giant branch (RGB star). It is well known that the number ratio of AGB to RGB stars near the TRGB should be about 1/3 for the intermediate age stars (Renzini 1992). Thus, there are more RGB populations below the TRGB. Evidence for the mass-loss from fainter sources is also seen in other panels. We see a bristle-shaped feature in (*N3* − *S11*) vs. *S11* panel, which is indicated by the arrow. The corresponding feature is marginal, but also seen in the (*S7* − *S11*) panel (indicated by the arrow).

Lebzelter et al. (2006) obtained low-resolution mid-infrared (7.6–21.7 μm) spectra of a star (V13) in the NGC 104 with Spitzer. The K_s-band luminosity of the star is fainter than the TRGB luminosity of NGC 104. They showed that the star is devoid of the 9.7 μm emission band feature of amorphous silicate, but it has broad emission features at 11.5 μm (likely to be Al_2O_3) and 13 μm (likely to be an Al–O stretching vibration). Aluminum oxide features have been detected from low mass-loss rate oxygen-rich red giants (Onaka et al. 1989; Kozasa & Sogawa 1997). Ita et al. (2007) suggested that the dust composition of V13 may be different from that of the usual mass-losing AGB star (i.e., the brighter group). As can be seen in figure 2, the IRC *S11* band includes all of these

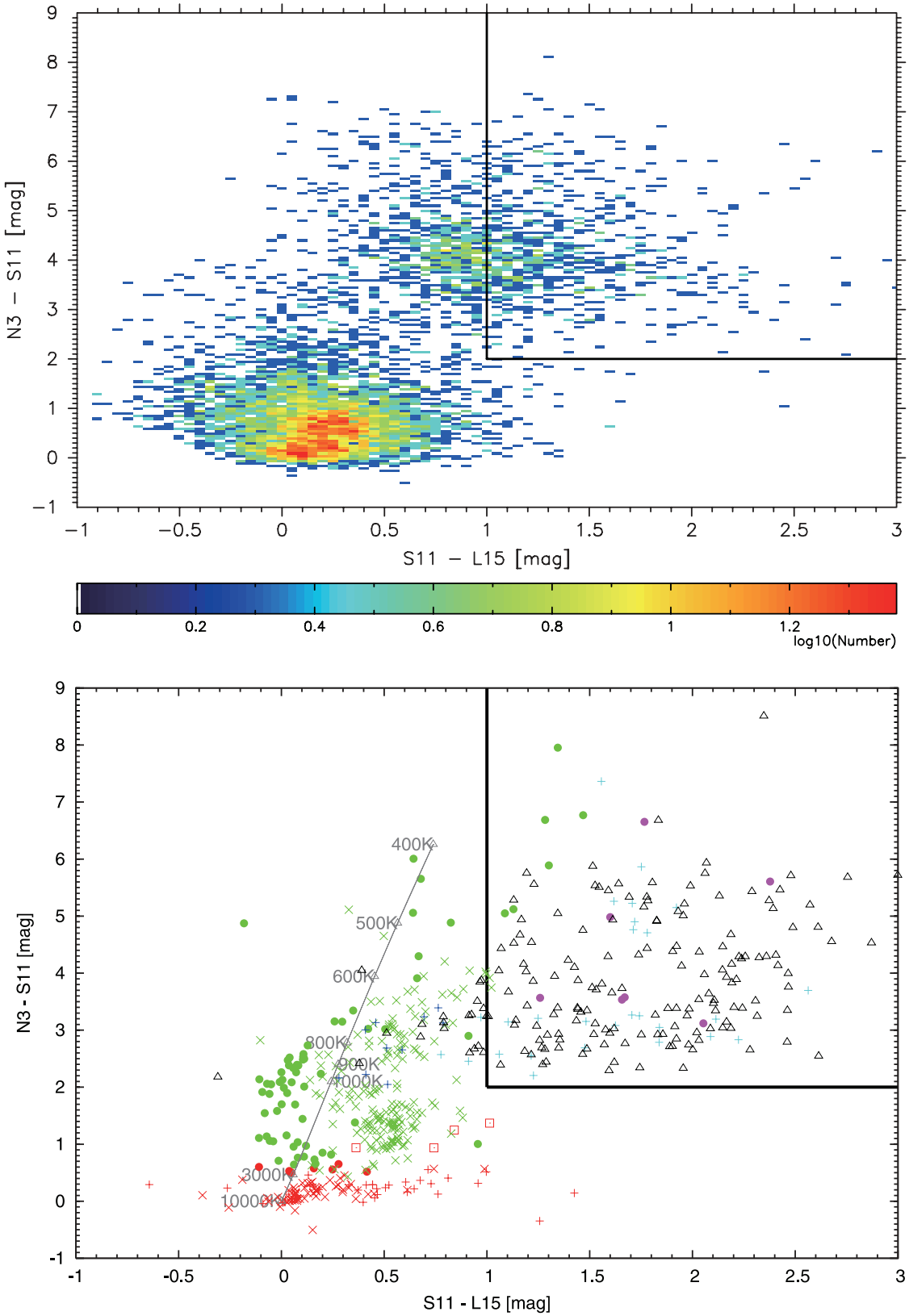

Fig. 8. (*S11*−*L15*) vs. (*N3*−*S11*) color–color diagram of AKARI/IRC sources (upper panel) and ISO SWS sources (lower panel). In the AKARI panel only sources with S/N > 5 are included, and the $(S11 - L15, N3 - S11)$ plane is binned by 0.05×0.05 mag^2 to calculate the number of sources in each bin. The number-density levels are logarithmic (see the wedge). The meanings of the marks and their colors in the ISO SWS panel are summarized in table 2. The solid gray line is a locus of the colors for blackbodies from a temperature of 400 to 10000 K. The solid black lines show criteria for selecting YSO candidates (see subsubsection 6.2.2).

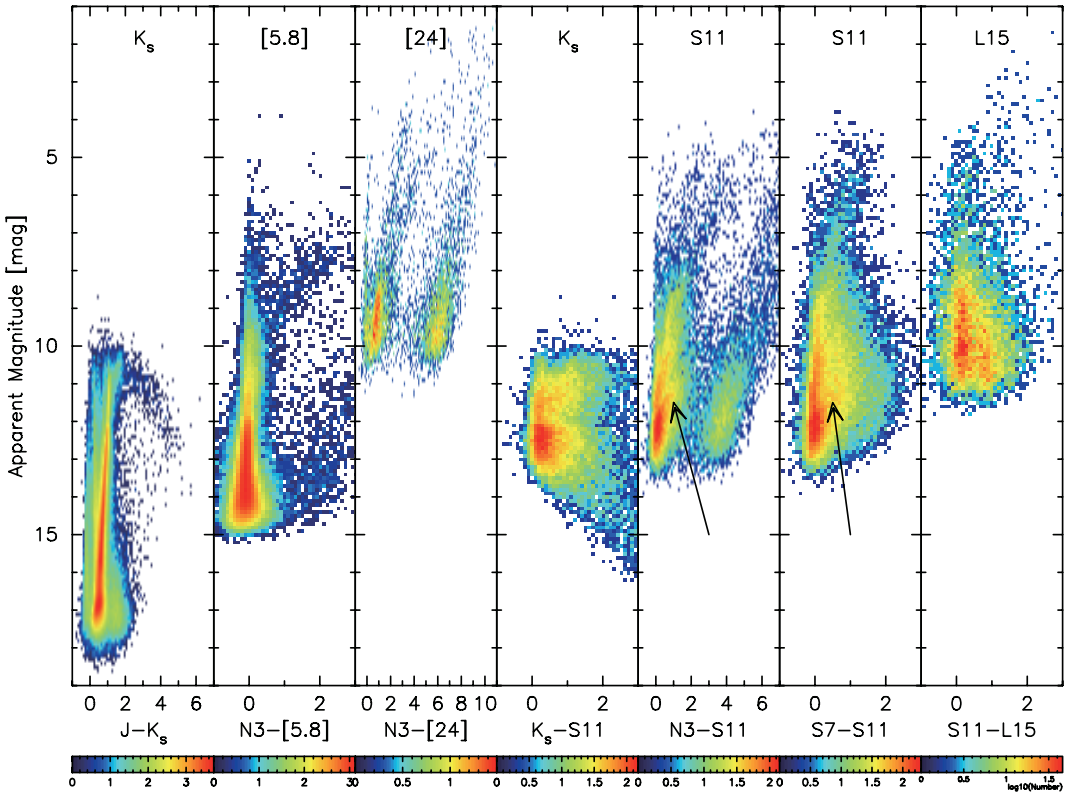

Fig. 9. Color–magnitude diagrams of AKARI LMC sources using several combinations of the IRC, IRAC, and IRSF/SIRIUS bands. The vertical axis is in apparent magnitude at the corresponding wavebands, which are indicated at the top of each panel. The arrows indicate the newly found feature, which can be attributed to red giants that have luminosities below the tip of the first red-giant branch.

emission features. Therefore, the feature indicated by the arrow in the (*N3* − *S11*) vs. *S11* panel may be attributed to those red giants with aluminum oxide dust, but without the silicate feature. Blum et al. (2006) identified a group of red, but faint, O-rich red giants in their (*[8.0]*–*[24]*) vs. *[8.0]* color–magnitude diagram. The sources with *S11* excess found in our (*N3* − *S11*) vs. *S11* panel may be similar to the red, but faint, O-rich red giants in Blum et al. (2006). Spectroscopic follow-up observations to identify the *S11* excess with the Al_2O_3 band would be interesting.

6.2.2. Carbon stars, dusty red giants, and YSO candidates on the CMDs

We identify carbon stars, dusty red giants, and YSO candidates by the following criteria, and estimate their location on the CMDs. The results are shown in figures 10 and 11.

- Optical carbon stars: As in subsubsection 5.4.3, we cross-identified our catalog with the carbon star catalog in the LMC (Kontizas et al. 2001) based on optical prism spectroscopy. They are shown by the green dots in figures 10 and 11.
- Dusty red giants: We select sources that satisfy the same conditions employed in subsubsection 5.4.3. We use the term "dusty red giants" here, but a significant fraction of the sources in this category can be actually infrared carbon stars, which are elusive in the above optical spectroscopic survey. According to Nikolaev and Weinberg (2000) stars with $(J - K_s) > 2.0$ in the LMC are primarily carbon-rich AGB stars. This can be explained as the J-band flux of carbon-rich mass-losing red giants are attenuated by C_2 and CN absorptions (Loidl et al. 2001). This criterion may also be satisfied by some dusty oxygen-rich AGB stars, but their number should be small compared to carbon stars. To confirm their circumstellar chemistry, our NP spectroscopic data would be effective. Sources in this category are shown by the red dots in figures 10 and 11.
- YSO candidates: Based on the color–color diagram (figure 8), we select sources that satisfy $(N3 - S11) > 2.0$ and $(S11 - L15) > 1.0$. As can be seen in the ISO SWS panel of figure 8, sources selected by this criteria include not only YSOs, but also other populations, such as PPNe and PNe. Also, background galaxies may have colors similar to sources in this category (see the following). Sources in this category are shown by the blue dots in figures 10 and 11.

Also, we calculated the bolometric magnitudes for sources that satisfy the following conditions:

- Sources detected in at least two of four optical (U, B, V, and I) bands.
- Sources detected in at least three of seven near-infrared (J, H, K_s, *N3*, *[3.6]*, *[4.5]*, and *[5.8]*) bands.
- Sources detected in at least three of four mid-infrared (*S7*, *[8.0]*, *S11*, and *L15*) bands.
- Sources detected in the *L24* and/or *[24]* bands.

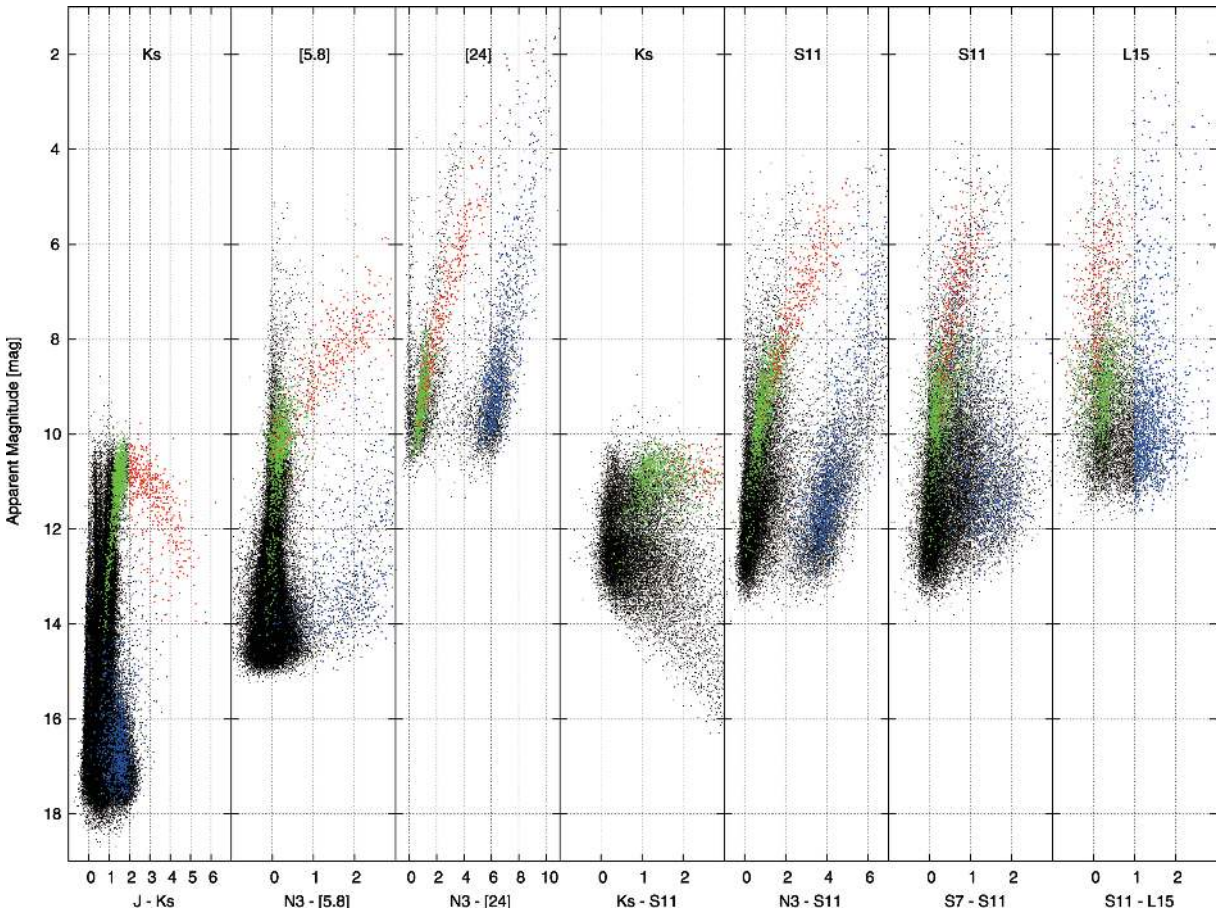

Fig. 10. The same as figure 9, but with spectroscopically confirmed carbon stars (green dots) by optical survey, candidates of dusty red giants (red dots), and candidates of YSOs (blue dots) are identified.

Table 3 summarizes the assumed zero-magnitude fluxes and their corresponding reference wavelengths that we used to calculate the flux densities. For the IRC bands, we used the zero magnitude fluxes and reference wavelengths listed in table 1. Since the zero magnitude fluxes for the IRSF/SIRIUS $JHK_{\rm s}$ bands are not officially determined, we converted the IRSF system magnitudes into the 2MASS system by using conversion equations provided in Kato et al. (2007) before calculating the flux densities. We then used a cubic spline to interpolate the spectral energy distributions and to integrate them from the shortest wavelength at which the flux is available to 24 μm to obtain the apparent bolometric magnitudes. Finally, we scaled them to the absolute magnitudes by assuming a distance modulus of 18.5 mag to the LMC. Figure 11 shows the result. For very red sources, such as galaxies, planetary nebulae, and extremely dusty AGB stars, the bolometric magnitudes may be underestimated to a large extent, because the fluxes longward of 24 μm are not included. Therefore, the bolometric magnitudes discussed here should be only lower limits.

It is apparent that optical carbon stars, dusty red giants, and YSO candidates are well separated from each other by color and luminosity. Except for the near-infrared CMD, YSO candidates have redder colors than that of the others, and dusty red giants are brighter in the mid-infrared bands than optical carbon stars. In the $(N3 - [24])$ vs. $[24]$ CMD, we see a group of sources that distribute along the vertical sequence around $(N3 - [24] \sim 0.0)$. These sources are likely to be foreground galactic stars that are classified as dwarf or giant. There is another feature in the diagram. We can see a sequence for dusty red giants (red dots), which grows toward the redder and brighter part of the CMD. Above the sequence, we see another branch that grows toward the redder and brighter part of the CMD. The brighter branch is clear in $(N3 - [24])$ vs. $[24]$ diagram, and is also seen in the $(N3 - S11)$ vs. $S11$ diagram. The corresponding bolometric magnitude CMDs tell us that most dusty red giants have absolute bolometric magnitudes ($M_{\rm bol}$) ranging from -4 to -5, while the sources on the brighter branch have $M_{\rm bol}$ brighter than -6 mag, and they are saturated in the IRSF/SIRIUS bands. It is suggested that sources on the brighter branch have stellar masses heavier than those of the sources on the sequence for dusty red giants. Their bolometric magnitudes agree well with the bolometric magnitudes for 88 red supergiants in the LMC (Oestreicher & Schmidt-Kaler 1998). Therefore, we conclude that the sources on the brighter branch are red supergiants.

As we suggest in subsubsection 6.1.2, the $(S11 - L15)$ color of dusty red giants once becomes blue during their evolution due to the growth of silicate or silicon carbide emission in the $S11$ band. In fact, most dusty red giants (red dots), if not all,

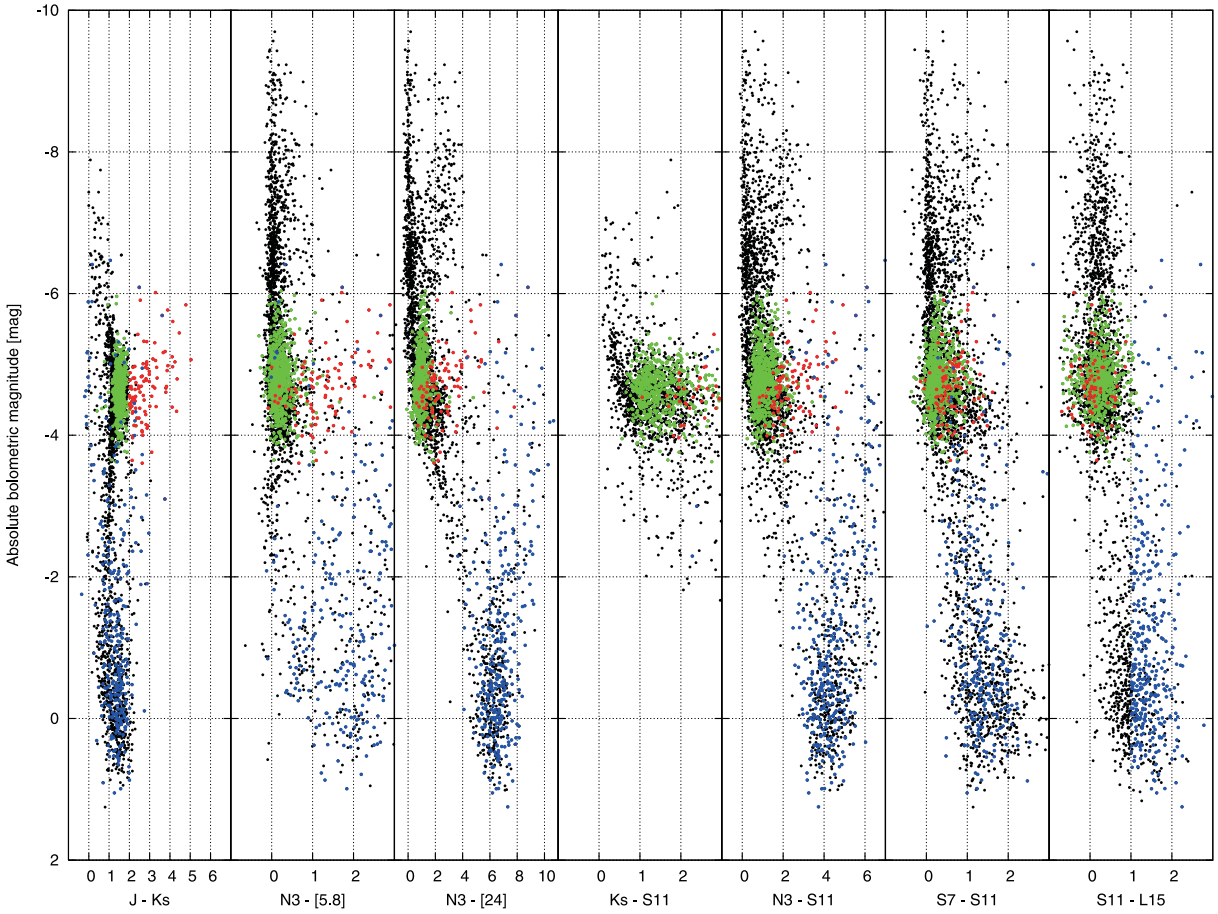

Fig. 11. Same as figure 10, but with the vertical axis in absolute bolometric magnitude. We assumed a distance modulus of 18.5 mag to the Large Magellanic Cloud. The meanings of colors of marks are the same in figure 10.

Table 3. Assumed zero magnitude fluxes and their corresponding reference wavelengths for the existing catalogs.

Wavebands	Zero magnitude flux [Jy]	Reference wavelength [μm]	Reference
U	1649	0.3745	Cohen et al. (2003)
B	4060	0.4481	〃
V	3723	0.5423	〃
I	2459	0.8071	〃
J	1594	1.235	Cohen, Wheaton, and Megeath (2003)
H	1024	1.662	〃
K_s	666.8	2.159	〃
[3.6]	280.9	3.550	IRAC Data Handbook*
[4.5]	179.7	4.493	〃
[5.8]	115.0	5.731	〃
[8.0]	64.1	7.872	〃
[24]	7.14	23.68	MIPS Data Handbook†

* IRAC Data Handbook, version 3.0, 2006 January 20, ⟨http://ssc.spitzer.caltech.edu/mips/dh/mipsdatahandbook3.3.pdf⟩.
† MIPS Data Handbook, version 3.3, ⟨http://ssc.spitzer.caltech.edu/mips/dh/mipsdatahandbook3.3.pdf⟩.

are bluer in ($S11 - L15$) than optical carbon stars (green dots).

6.2.3. Background galaxies and foreground Milky Way sources

To estimate how many background galaxies and foreground sources are expected in the CMDs, we used the leftover NIR and MIRS data that were kindly offered by the AKARI stellar working group (PI. Y. Nakada). The data were obtained when they took MIRL images of globular clusters. MIRL observations concurrently yield NIR and MIRS images that observe $25'$ away from the MIRL center (= target center). Also they observed some local group galaxies, and took several reference images for them, which were about 1° away from the target centers. These reference data were also included in the following analysis. Among those offered by AKARI stellar working group, we selected fields whose absolute value of the galactic latitudes $|b|$ were in the range of $30^\circ < |b| < 40^\circ$, which are comparable to the mean value of the AKARI LMC survey regions ($|b| \sim 32.^\circ5$). We reduced the data in the same way as we did for the LMC survey. The total area of the reference fields is 500 arcmin^2. The coordinates of the referenced fields are listed in table 4. We checked IRAS 24, 60, and 100 μm images of the corresponding coordinates, and found no appreciable indication of star forming regions and molecular clouds.

Using the data of the reference fields, we made CMDs that can be directly compared to figures 9 and 10. They are shown in figure 12. Most, if not all, of the sources in figure 12 are expected to be background galaxies and foreground Milky Way stars, with a few possibility of stars in the outer skirts of target globular clusters. We checked the tidal radii of the target globular clusters (Harris 1996), and they are about a half of the offset value of $25'$. In the following analysis, we ignore the small contribution from stars in the outer skirts of each globular cluster. Due to the high source density, particularly in the central part of the LMC, the completeness limit of the LMC survey data must be shallower than that of the reference fields. Therefore, we only counted the number of sources that satisfied the following conditions:

(1) For presumable background galaxy:

- $(N3 - S11) > 2$ [mag]
- $10 < S11$ [mag] < 12.2

(2) For presumable foreground stars:

- $(N3 - S11) < 2$ [mag]
- $9 < S11$ [mag] < 12.2

We then found 72 background galaxies and 26 foreground stars in the reference fields. The differences in number counts for both populations among the reference fields were small. These results imply that we can expect about 500 background galaxies and 190 foreground stars in a square degree. This estimation agrees with the Spitzer results (Fazio et al. 2004b; Meixner et al. 2006). On the other hand, we found 4483 and 14951 sources in our catalog (compiled from 10 deg^2 survey data) that satisfied the above conditions, respectively. Therefore, most, if not all, of the sources that satisfy the condition (1) in our catalog should be background galaxies. Meanwhile, the fraction of foreground stars in the sources that satisfy condition (2) is estimated to be about 13%.

Table 4. Galactic coordinates of reference fields.

ID	Longitude (°)	Latitude (°)
1	86.26824	34.38021
2	87.56487	34.71097
3	87.67876	35.02329
4	244.41766	−34.71058
5	68.25446	35.19998

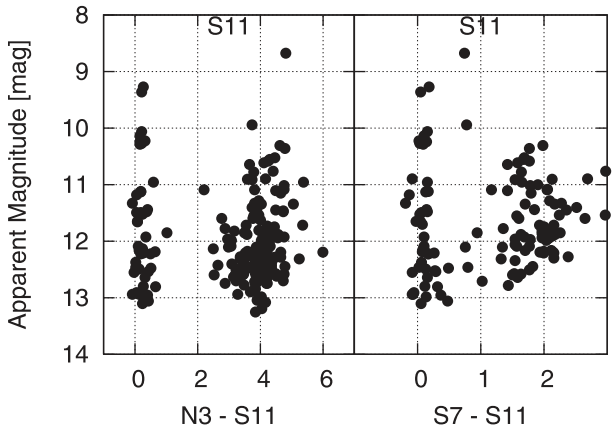

Fig. 12. Color–magnitude diagrams for sources in reference fields.

7. Summary

We carried out an imaging and spectroscopic survey of a 10 deg^2 area of the LMC using IRC onboard AKARI. In this paper we discuss the imaging data obtained in the survey, and describe a preliminary photometric catalog of bright point sources. The first point-source catalog is planned to be released to the public in 2009. We cross-identified our catalog with the existing optical, near-infrared, and mid-infrared photometry catalogs, and used the combined data to build color–magnitude diagrams using several combinations of interesting wavebands, and also to calculate the absolute bolometric magnitudes. By virtue of the *S11* and *L15* bands, which are unique to IRC, we found new interesting features in the color–magnitude diagrams. The present IRC data and the upcoming results from AKARI All-Sky Survey together with existing radio and near-infrared ground-based observational results will provide a significant database to study the star-formation history and material circulation within a galaxy.

We thank the referee for providing constructive comments and helping to improve this paper. Y.I. thank Dr. Gregory C. Sloan for helpful comments at the IAU Symposium 256 held in the Keele University. We acknowledge the use of Spitzer SAGE-LMC data in the assessment of the AKARI LMC results, and thank the SAGE-LMC team, led by Dr. Margaret Meixner, for early access to data for this purpose. AKARI is a JAXA project with the participation of ESA. We are grateful to the members of AKARI stellar working

group for providing us with their data, and also for valuable discussions that helped to improve this paper. This work is supported by a Grant-in-Aid for Scientific Research (A) No. 18204014 from Japan Society for the Promotion of Science and also supported by a Grant-in-Aid for Encouragement of Young Scientists (B) No. 17740120 from the Ministry of Education, Culture, Sports, Science and Technology of Japan. This work is partly supported by a JSPS grant (grant number 16204013). This publication makes use of data products from the Two Micron All Sky Survey, which is a joint project of the University of Massachusetts and the Infrared Processing and Analysis Center/California Institute of Technology, funded by the US National Aeronautics and Space Administration and the National Science Foundation. This research has made use of the NASA/IPAC Infrared Science Archive, which is operated by the Jet Propulsion Laboratory, California Institute of Technology, under contract with the National Aeronautics and Space Administration.

References

Aguirre, J. E., et al. 2003, ApJ, 596, 273
Arendt, R. G., Dwek, E., & Moseley, S. H. 1999, ApJ, 521, 234
Benjamin, R. A., et al. 2003, PASP, 115, 953
Bertin, E., & Arnouts, S. 1996, A&AS, 117, 393
Blum, R. D., et al. 2006, AJ, 132, 2034
Bolatto, A. D., et al. 2007, ApJ, 655, 212
Bolatto, A. D., Jackson, J. M., Israel, F. P., Zhang, X., & Sungeun, K. 2000, ApJ, 545, 234
Borkowski, K. J., et al. 2006, ApJ, 642, L141
Chan, K.-W., & Onaka, T. 2000, ApJ, 533, L33
Cioni, M.-R., et al. 2000a, A&AS, 144, 235
Cioni, M.-R. I., van der Marel, R. P., Loup, C., & Habing, H. J. 2000b, A&A, 359, 601
Clayton, D. D., Denault, E. A.-N., & Meyer, B. S. 2001, ApJ, 562, 480
Cohen, M., Megeath, S. T., Hammersley, P. L., Martín-Luis, F., & Stauffer, J. 2003, AJ, 125, 2645
Cohen, M., Wheaton, W. A., & Megeath, S. T. 2003, AJ, 126, 1090
Cox, N. L. J, & Spaans, M. 2006, A&A, 451, 973
Crosas, M., & Menten, K. M. 1997, ApJ, 483, 913
Douvion, T., Lagage, P. O., Casarsky, C. J., & Dwek, E. 2001, A&A, 373, 281
Dwek, E. 1986, ApJ, 302, 363
Dwek, E. 1998, ApJ, 501, 643
Egan, M. P., et al. 2003, in Air Force Research Laboratory Technical Report, Vol. AFRL-VS-TR-2003-1589
Fazio, G. G., et al. 2004a, ApJS, 154, 10
Fazio, G. G., et al. 2004b, ApJS, 154, 39
Feast, M. W., & Walker, A. R. 1987, ARA&A, 25, 345
Filipović, M. D., Jones, P. A., White, G. L., & Haynes, R. F. 1998, A&AS, 130, 441
Fukui, Y. 2005, IAU Symp., 227, 328
Gaustad, J. E., McCollough, P. R., Rosing, W., & Van Buren, D. 2001, PASP, 113, 1326
Götz, D., Mereghetti, S., Merlini, D., Sidoli, L., & Belloni, T. 2006, A&A, 448, 873
Haberl, F., Dennerl, K., & Pietsch, W. 2003, A&A, 406, 471
Haberl, F., & Pietsch, W. 1999, A&AS, 139, 277
Harris, W. E. 1996, AJ, 112, 1487
Hosokawa, T., & Inutsuka, S. 2006, ApJ, 646, 240
Ishihara, D., et al. 2006, PASP, 118, 324
Israel, F. P., et al. 1986, in Light on Dark Matter: Proc. of the First IRAS Conf., ed. F. P. Israel, (Dorrecht: D. Reidel Publishing), 383
Ita, Y., et al. 2004a, MNRAS, 347, 720
Ita, Y., et al. 2004b, MNRAS, 353, 705
Ita, Y., et al. 2007, PASJ, 59, S437
Jones, A. P., Tielens, A. G. G. M., & Hollenbach, D. J. 1994, ApJ, 433, 797
Jones, A. P., Tielens, A. G. G. M., Hollenbach, D. J., & McKee, C. F. 1996, ApJ, 469, 740
Kato, D., et al. 2007, PASJ, 59, 615
Kawada, M., et al. 2007, PASJ, 59, S389
Kennicutt, R. C., Jr., & Hodge, P. W. 1986, ApJ, 306, 130
Kepler, S. O., Kleinman, S. J., Nitta, A., Koester, D., Castanheira, B. G., Giovannini, O., Costa, A. F. M., & Althaus, L. 2007, MNRAS, 375, 1315
Kim, S., Staveley-Smith, L., Dopita, M. A., Freeman, K. C., Sault, R. J., Kesteven, M. J., & McConnell, D. 1998, ApJ, 503, 674
Kontizas, E., Dapergolas, A., Morgan, D. H., & Kontizas, M. 2001, A&A, 369, 932
Koo, B.-C., et al. 2007, PASJ, 59, S455
Koo, B.-C., et al. 2008, ApJ, 673, L147
Koornneef, J. 1982, A&A, 107, 247
Kozasa, T., & Sogawa, H. 1997, Ap&SS, 251, 165
Kraemer, K. E., Sloan, G. C., Price, S. D., & Walker, H. J. 2002, ApJS, 140, 389
Krause, O., Krause, O., Birkmann, S. M., Rieke, G. H., Lemke, D., Klaas, U., Hines, D. C., & Gordon, K. D. 2004, Nature, 432, 596
Kumai, Y., Basu, B., & Fujimoto, M. 1993, ApJ, 404, 144
Lebzelter, Th., Posch, Th., Hinkle, K., Wood, P. R., & Bouwman, J. 2006, ApJ, 653, L145
Loidl, R., Lançon, A., & Jørgensen, U. G. 2001, A&A, 371, 1065
Long, K. S., Helfand, D. J., & Grabelsky, D. A. 1981, ApJ, 248, 925
Luks, Th., & Rohlfs, K. 1992, A&A, 263, 41
Matsuhara, H., et al. 2007, PASJ, 59, S543
Meikle, W. P. S., et al. 2007, ApJ, 665, 608
Meixner, M., et al. 2006, AJ, 132, 2288
Mizuno, N., et al. 2001, PASJ, 53, 971
Mochizuki, K., et al. 1994, ApJ, 430, L37
Murakami, H., et al. 2007, PASJ, 59, S369
Nikolaev, S., & Weinberg, M. D. 2000, ApJ, 542, 804
Oestreicher, M. O., & Schmidt-Kaler, Th. 1998, MNRAS, 299, 625
Ohyama, Y., et al. 2007, PASJ, 59, S411
Onaka, T. 2000, Adv. Sp. Res., 25, 2167
Onaka, T., et al. 2007, PASJ, 59, S401
Onaka, T., De Jong, T., & Willems, F. J. 1989, A&A, 218, 169
Onaka, T., Roelling, T. L., Okada, Y., & Chan, K.-W. 2008, ASP Conf. Ser., 381, 80
Perryman, M. A. C., et al. 1997, A&A, 323, L49
Ramdani, A., & Jorissen, A. 2001, A&AS, 372, 85
Renzini, A. 1992, in IAU Symp. 149, The Stellar Populations of Galaxies, ed. B. Barbuy & A. Renzini, (Dordrecht: Kluwer), 325
Rho, J., et al. 2008, ApJ, 673, 271
Rieke, G. H., et al. 2004, ApJS, 154, 25
Sakon, I., Onaka, T., Ishihara, D., Ootsubo, T., Yamamura, I., Tanabé, T., & Roellig, T. L. 2004, ApJ, 609, 203

Sakon, I., Onaka, T., Kaneda, H., Tokura, D., Tajiri, Y. Y., Takahashi, H., Kato, D., & Onishi, T. 2005, IAUS, 235, 145
Sasaki, M., Haberl, F., & Pietsch, W. 2000, A&AS, 143, 391
Seok, J. Y., et al. 2008, PASJ, 60, S453
Skrutskie, M. F., et al. 2006, AJ, 131, 1163
Sloan, G. C., Kathleen, E., Kraemer, K. E., Price, S. D., & Shipman, R. F. 2003, ApJS, 147, 379
Smith, A. M., Cornett, R. H., & Hill, R. S. 1987, ApJ, 320, 609
Tanabé, T., et al. 2008, PASJ, 60, S375
Temim, T., et al. 2006, AJ, 132, 1610
Todini, P., & Ferrara, A. 2001, MNRAS, 325, 726
Udalski, A., Kubiak, M., & Szymański, M. 1997, Acta Astron., 47, 319
van Loon, J. Th., et al. 2005, MNRAS, 364, 71
Werner, M. W., et al. 2004, ApJS, 154, 1
Williams, B. J., et al. 2006, ApJ, 652, 33
Williams, R. M., Chu, Y.-H., & Gruendl, R. 2006, AJ, 132, 1877
Yamaguchi, R., Mizuno, N., Onishi, T., Mizuno, A., & Fukui, Y. 2001, PASJ, 53, 959
Yamamura, I., & de Jong, T. 2000, in ISO beyond the Peaks: The 2nd ISO Workshop on Analytical Spectroscopy. ed. A. Salama, M. F. Kessler, K. Leech, & B. Schulz, (ESA-SP 456), (Noordwijk: ESA), 155
Zaritsky, D., Harris, J., Thompson, I. B., & Grebel, E. K. 2004, AJ, 128, 1606
Żebruń, K., et al. 2001, Acta Astron., 51, 317